Nanoscale Horizons

ROYAL SOCIETY OF CHEMISTRY

COMMUNICATION

View Article Online
View Journal | View Issue

Cite this: *Nanoscale Horiz.*, 2025, **10**, 3051

Received 15th July 2025,
Accepted 3rd September 2025

DOI: 10.1039/d5nh00496a

rsc.li/nanoscale-horizons

Advances in the direct conversion of CH_4 and CO_2 into acetic acid over bimetallic catalysts supported on H-ZSM-5

Gabriel F. Lopes, Alessandra F. Lucrédio, Luiz H. Vieira * and Elisabete M. Assaf *

This study developed heterogeneous catalysts composed of ZnO and CeO_2 supported on H-ZSM-5 for the direct conversion of methane (CH_4) and carbon dioxide (CO_2) into acetic acid. The acid–base and electronic properties were modulated through oxide impregnation and reduction, aiming to create active sites capable of simultaneously activating both reactants. The samples were characterized by XRD, N_2 physisorption, HRTEM/EDS, NH_3-TPD, CO_2-TPD, TPR, FTIR, XPS, CO_2-DRIFTS, and TGA, and tested in a batch reactor at 300 °C and 10 bar. The catalyst lifetime was evaluated through stability testing. The zeolite framework was preserved, although its properties were modified, resulting in improved CH_4 and CO_2 activation. The reduced catalyst exhibited a high surface area and an efficient distribution of acidic and basic sites, achieving an acetic acid productivity of 1473.40 μmol g^{-1} h^{-1} and a conversion rate of 35.12%. The results surpassed those of previous studies, highlighting the potential of the Zn–Ce/H-ZSM-5 system for biogas valorization and greenhouse gas mitigation.

New concepts

The direct transformation of CH_4 and CO_2 into acetic acid marks an exciting step forward in biogas valorization, though it faces challenges due to the difficulty of activating both molecules simultaneously. This study presents a novel catalytic approach that leverages the synergistic tuning of acidity and basicity in a zeolite modified with metal oxides. Reductive treatment creates oxygen vacancies and active metallic species, facilitating the adsorption and conversion of reactants. In addition to the catalytic innovation, the research emphasizes the importance of combining ^{1}H NMR and HPLC techniques, which enabled precise measurement of acetic acid produced in batch reactors. Complementary analysis using TGA under N_2 and FTIR confirmed the presence of the product within the catalyst pores and on surfaces. This strategy not only considers material composition but also controls the chemical state of metal oxides and their interaction with Brønsted acid sites. The resulting productivity of 1473.40 μmol g^{-1} h^{-1} surpasses previously reported values and underscores the critical role of acid–base properties, modulated by reduction, in synthesizing acetic acid from greenhouse gases.

Introduction

One of the primary causes of climate change is the emission of greenhouse gases, posing a significant global-scale challenge. It is widely recognized that the gradual increase of carbon dioxide (CO_2) in the atmosphere has contributed to global warming, highlighting the importance of reducing its atmospheric concentration.[1,2]

As an alternative, the conversion of biogas, composed of CO_2 and methane (CH_4), can be considered, as both gases can be used as feedstock for the production of acetic acid, a compound employed in the manufacture of acetates, anhydrides, acrylates, organic acids, pharmaceutical solvents, food processing, among other applications.[2]

The conversion of CO_2 and CH_4 into other compounds not only helps mitigate climate change but also reinforces the application of sustainable catalysis.[3] CO_2 and CH_4 molecules are thermodynamically stable and require high energy for activation, representing a challenge for catalyst performance, which depends on the nature of the active phase, the support, and the reaction conditions. Additionally, the yield of acetic acid depends on the presence of Brønsted and Lewis acid sites.[4] One of the main challenges of this reaction is the need to overcome high thermodynamic barriers for CH_4 activation, requiring high temperatures to reduce the activation energy.[5]

Ding *et al.* (2007)[6] studied Pd and Rh catalysts supported on SiO_2 for the synthesis of acetic acid from CH_4 and CO_2. With 2% Pd, the maximum acetic acid yield was 38.38 μmol g^{-1} h^{-1} at 200 °C, and with 2% Rh, it was 12.26 μmol g^{-1} h^{-1} at 400 °C, under continuous flow of CH_4 (85 mL min^{-1}) and CO_2 (85 mL min^{-1}) over 20 cycles of 5 hours. A Cu/ZnO catalyst was studied in a wet reduction process activated by photons at 25 °C and 20 bar, yielding 411.6 μmol g^{-1} h^{-1} of acetic acid with a selectivity of 89.5%.[7]

Dual-component catalysts (ZnO and CeO_2) supported on montmorillonite showed the formation of 350 μmol g^{-1} h^{-1}

Department of Physical Chemistry, São Carlos Institute of Chemistry, University of São Paulo, Brazil. E-mail: lhvieira@iqsc.usp.br, eassaf@iqsc.usp.br

of acetic acid, highlighting CH_4 activation on ZnO and CO_2 activation on CeO_2.[8] A bimetallic catalyst, Cu^0-K^+-ZSM-5, produced 395 μmol g^{-1} h^{-1} of acetic acid, demonstrating the efficiency of reduced metals.[9]

In this work, Zn- and Ce-based catalysts in oxide and reduced forms, supported on H-ZSM-5, were investigated, aiming to provide basicity for CO_2 activation on a support with acidic characteristics.

Results and discussion

The catalysts were synthesized through the wet impregnation of metal nitrates to achieve the desired oxide concentrations of 0.38 wt% CeO_2 and 1.90 wt% ZnO. To prepare the oxide catalyst, the calcination temperature (550 °C) was determined by thermogravimetric analysis (TGA), based on the thermal stabilization profile of the material.[10] The H-ZSM-5 support (Fig. 1a) exhibits two main mass loss events: the first, up to 100 °C, corresponds to a 3.80% mass loss, associated with the removal of strongly bound structural water from the zeolite; and the second, a 5.80% mass loss, is related to surface dehydroxylation. With the incorporation of ZnO and CeO_2 (Fig. 1b), a significant increase in mass loss is observed throughout the thermal analysis. The fresh material exhibits an initial mass loss of 4.20%, which is attributed to the removal of structural water, like the support. Additionally, it exhibits a second mass loss of up to 7.80%, associated with the removal of hydration water from nitrates during their decomposition into metal oxides, reaching thermal stability at 550 °C with a total mass loss of 8.10%.

To prepare the reduced catalyst, temperature programmed reduction with hydrogen (TPR-H_2) was carried out on the calcined sample to determine the optimal reduction temperature. The TPR profiles (Fig. 1c) revealed three distinct hydrogen consumption events, with a total uptake of 54.91 μmolH_2 g^{-1}. The first reduction peak, at 385 °C, was attributed to the surface reduction of Ce^{4+} to Ce^{3+} in the CeO_2 nanoparticles, corresponding to 1.86 μmolH_2 g^{-1}, with 8.42% reducibility, which also represents the degree of oxygen vacancy formation available during the reaction. The last one, at 716 °C, corresponds to the reduction of bulk Ce^{4+}, with a hydrogen uptake of 4.59 μmolH_2 g^{-1}.[11]

The second peak, spanning the range from 250 to 900 °C, was associated with the reduction of ZnO to $Zn^{\delta+}$, with a hydrogen uptake of 42.02 μmolH_2 g^{-1}. Based on TPR profile, a temperature of 570 °C was selected as the optimal reduction condition for the catalyst.[12] This temperature ensures ZnO and surface CeO_2 reduction while avoiding higher temperature ranges that could compromise the thermal stability of the catalyst. This reduction process promotes the release of surface oxygen atoms, leading to the formation of oxygen vacancies.[13]

To confirm the formation of oxygen vacancies, and consequently the generation of Ce^{3+} species and their efficiency in CO_2 adsorption, *in situ* DRIFTS measurements were carried out on the fresh and pre-reduced samples (Fig. 2). The reduced sample exhibited more intense spectral variations during CO_2 exposure, indicating a higher adsorption capacity.

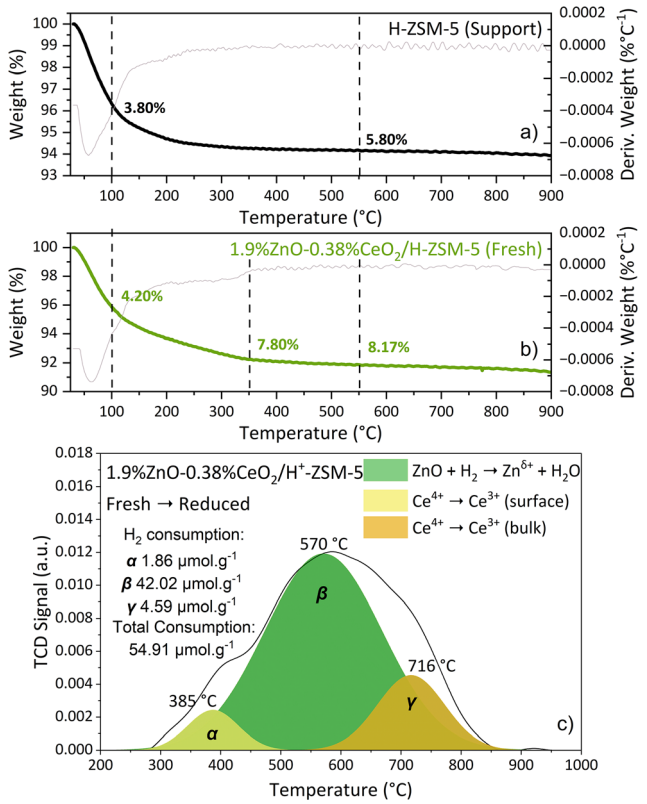

Fig. 1 Thermogravimetric analysis (a and b) and temperature programmed reduction (H_2-TPR) (c) of catalysts.

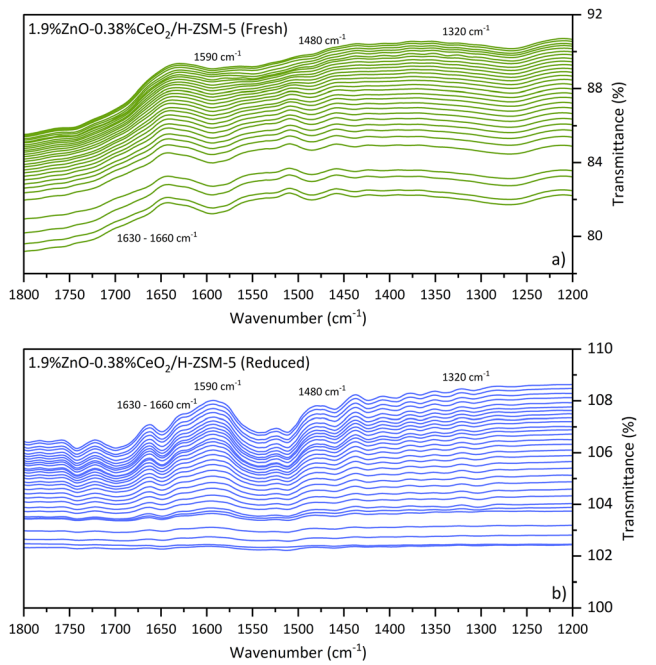

Fig. 2 DRIFTS spectra in the carbonate formation region for Ce^{4+} and Ce^{3+} in the fresh (a) and reduced (b) catalyst.

The bands detected at 1630–1660 cm^{-1} are assigned to bicarbonate species (HCO_3^-), resulting from the interaction of CO_2 with Brønsted hydroxyls present in the zeolite. The growth of bands at 1590 cm^{-1} and 1320 cm^{-1}, characteristic of bidentate carbonates, as well as the band at 1480 cm^{-1}, attributed to monodentate carbonates, provides evidence of CO_2 adsorption on CeO_2 sites.[14,15] The higher intensity of these signals in the reduced sample suggests that the reductive treatment favored the formation of oxygen vacancies in CeO_2 (Ce^{3+}), which act as active centers for carbonate stabilization. These results confirm that the reductive treatment plays a crucial role in activating the catalyst surface, increasing both the density and diversity of active sites capable of interacting with CO_2.

X-ray diffraction (XRD) analysis was performed to investigate the crystallinity of the zeolite and the presence of crystalline phases of ZnO and CeO_2 in the impregnated materials. In Fig. 3, the diffractogram shows the characteristic peaks of the H-ZSM-5 structure, matching the JCPDS standard 44-3, confirming the preservation of its crystalline structure.[16]

For the fresh catalyst, the characteristic zeolite peaks remain visible, indicating that the impregnation with ZnO and CeO_2 did not compromise the crystalline framework. For the reduced catalyst, the peaks are also preserved, showing that the zeolite structure remains stable after reduction. However, no defined peaks attributable to ZnO or CeO_2 are observed, based on JCPDS patterns 36-1451 and 34-0394, respectively, where diffraction peaks were expected at 31.72° (100), 34.38° (002), 36.20° (101), 47.48° (102), 56.54° (110), 62.80° (103), and 67.90° (112) for ZnO,[17] and 28.34° (111), 31.52° (200), 47.34° (220), and 56.41° (311) for CeO_2.[18] The absence of such peaks is attributed to the impregnated amounts being below the XRD detection limit and the high dispersion of the oxides.

To complement the XRD results, HRTEM and EDS analyses were carried out. Regarding the support (Fig. 5a and Fig. S1), crystals with irregular hexagonal morphology and well-defined edges are observed, typical of MFI zeolite structures.[19] Lattice fringes with average spacings of 0.52 and 0.55 nm are visible, characteristic of the microporosity of the zeolite.[20] The EDS mapping of the support (Fig. 5b and Fig. S2) reveals the homogeneous distribution of Si (cyan) and Al (yellow) throughout the crystal, confirming the structural integrity and a Si/Al ratio of 31. In the fresh catalyst (Fig. 5c and Fig. S3), the presence of CeO_2 nanoparticles dispersed on the zeolite support is evident, with an average diameter of 2.8 nm.[21] ZnO, on the other hand, is not directly visible in the HRTEM images due to its high dispersion and relatively smaller size, or even due to its partial exchange with H^+ from the zeolite during the material synthesis.[22] Furthermore, EDS elemental mapping (Fig. 5d and Fig. S4) shows a homogeneous distribution of Zn, reinforcing its high dispersion and incorporation into the zeolite pores. However, quantitatively, the concentrations obtained were 1.06 wt% ZnO and 2.01 wt% CeO_2, which deviated from the expected values assigned during synthesis, namely 1.9 wt% ZnO and 0.38 wt% CeO_2 (Fig. S8). In the reduced catalyst (Fig. 5e and Fig. S5), CeO_2 nanoparticles slightly increased, reaching an average size of 5.0 nm, attributed to coalescence during the reduction step.[23] EDS mapping (Fig. 5f and Fig. S6) indicates that Zn and Ce remain well-distributed, suggesting that despite Ce nanoparticle growth, no segregation occurred.

The isotherm of the support is shown in Fig. 4a, exhibiting a combination of type I and IV isotherms, typical of micro-mesoporous structures with H4-type hysteresis.[24] The support presents a specific surface area of 213 $m^2\ g^{-1}$, a pore volume of 0.133 $cm^3\ g^{-1}$ and an average pore diameter of 1.50 nm, referring to interparticle porosity (Table 1).

The fresh catalyst (Fig. 4b) exhibits a similar behavior. After impregnation with ZnO and CeO_2, a reduction in surface area and pore volume is observed, while the average pore diameter

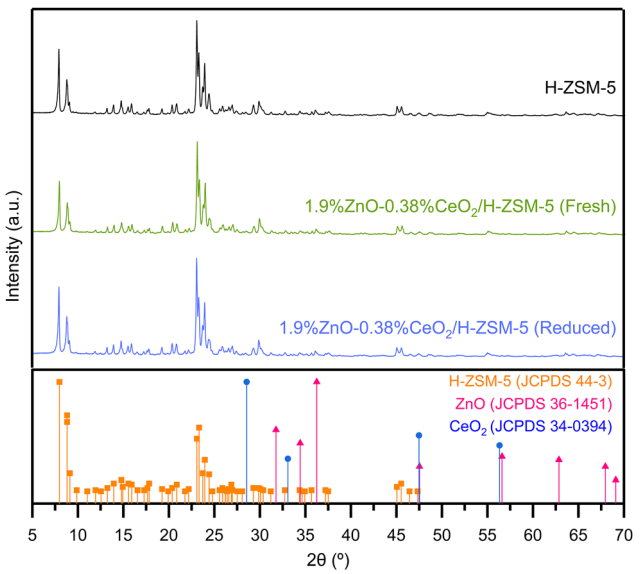

Fig. 3 X-ray diffractometry of the support and the fresh and reduced catalyst.

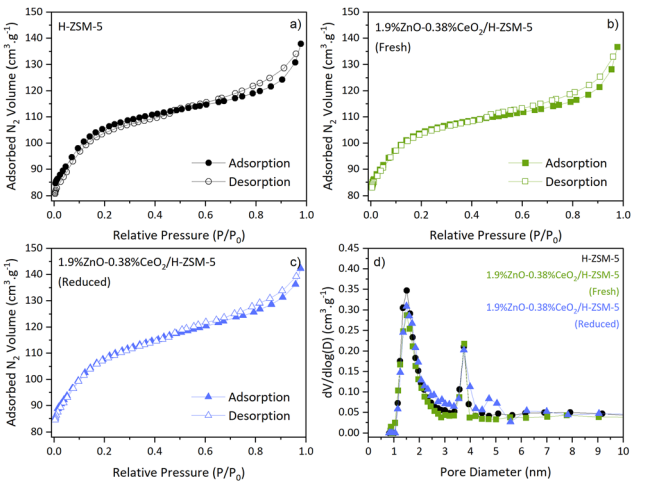

Fig. 4 N_2 physisorption isotherms (a–c) and pore size distributions (d) for the support and the catalysts.

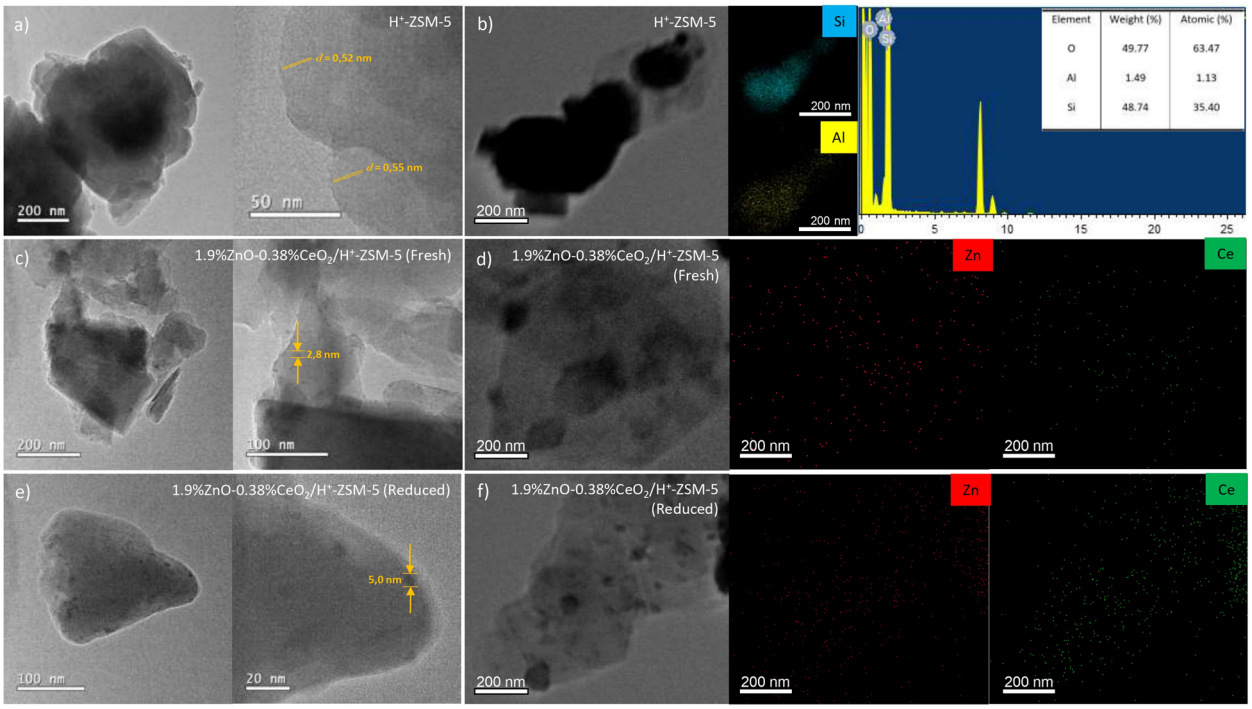

Fig. 5 High-resolution transmission electron microscopy (HRTEM) and elemental mapping by energy-dispersive X-ray spectroscopy (EDS) of the support (a and b) and the fresh (c and d) and reduced (e and f) catalyst.

Table 1 Textural properties of the catalysts

Catalyst	Surface area ($m^2\ g^{-1}$)	Pore volum ($cm^3\ g^{-1}$)	Pore diameter (nm)
H-ZSM-5	213	0.133	1.50
Fresh	192	0.123	1.51
Reduced	204	0.132	1.49

Table 2 Acetic acid productivity and conversion

	Acetic acid ($\mu mol\ g^{-1}\ h^{-1}$)		Conversion (%)	
Catalyst	^{1}H NMR	HPLC	^{1}H NMR	HPLC
H-ZSM-5	0.00	0.00	0.00	0.00
Fresh	120.03	78.00	2.86	1.86
Reduced	1473.40	1273.10	35.12	30.34

remains constant.[25] These reductions are attributed to pore blockage by the metal precursors.

In the reduced catalyst (Fig. 4c), a more pronounced hysteresis behavior is observed in the mesoporous region, along with an increase in specific surface area, pore volume of 0.132 $cm^3\ g^{-1}$, and an average pore diameter of 1.49 nm.

This behavior is related to the redistribution of metal oxides within the zeolite matrix after reduction, which unblocks previously obstructed pores or restructures the surface, exposing new accessible areas.

The pore diameter distribution (Fig. 4d) shows that the materials exhibit peaks in the range of 2 to 5 nm,[26] indicating the presence of mesopores. The reduced sample displays a more intense peak at 3.5 nm, attributed to a narrowing of the pore size distribution resulting from particle growth after reduction.

The fresh and reduced catalysts were applied to the reaction, and the results are shown in Table 2. The reduced catalyst demonstrated a considerable increase in performance in terms of acetic acid production compared to the fresh catalyst, while the support exhibited no activity.

In the ^{1}H NMR analysis (Fig. 6a), it is observed that the support does not show significant peaks in the studied region,

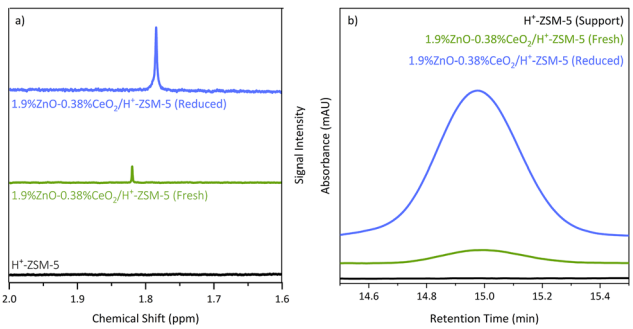

Fig. 6 ^{1}H NMR spectra (a) and HPLC chromatograms (b) in the acetic acid region.

indicating the absence of acetic acid. On the other hand, the fresh catalyst displays well-defined peaks around 1.8 ppm, indicating catalytic activity, achieving 120.03 $\mu mol\ g^{-1}\ h^{-1}$ of acetic acid productivity. The HPLC results (Fig. 6b) corroborate the ^{1}H NMR data discussed earlier. Again, the support shows no significant peaks, confirming the absence of acetic acid. The fresh catalyst, however, exhibits a well-defined peak with a retention time around 15 minutes, consistent with the acetic

acid detected by ^{1}H NMR, with a quantified formation of 78 μmol g^{-1} h^{-1}. The reduced catalyst, in turn, shows characteristic and more intense peaks in both ^{1}H NMR and HPLC analyses, quantified at 1473.40 μmol g^{-1} h^{-1} and 1273.10 μmol g^{-1} h^{-1}, respectively.

Overall, the data indicate that the presence of metal oxides is crucial for promoting catalytic activity. Furthermore, the reduced catalyst exhibited remarkable efficiency, with conversions of 35.12% and 30.34% based on ^{1}H NMR and HPLC data, respectively. This suggests that Brønsted acidity, combined with the precursors in their reduced forms, plays a fundamental role in catalytic activity, associated with structural and electronic modifications, as discussed in the N_2 physisorption and HRTEM analyses. The reduction of CeO_2 leads to the formation of oxygen vacancies, which act as active sites for CO_2 activation, while the formation of isolated Zn species contributes to CH_4 activation.[27] These synergistic effects favor a more efficient reaction mechanism compared to the fresh sample, whose activity is predominantly limited to the formation of surface carbonates.

Given the catalytic results obtained, the combination of ZnO and CeO_2 supported on H-ZSM-5 proved effective for the direct conversion of CH_4 and CO_2 into acetic acid, achieving productivities higher than those reported in the literature. Although Shavi *et al.* (2018)[8] introduced the concept of dual sites to avoid adsorption competition between CH_4 and CO_2, the absence of Brønsted acidity limited the catalytic conversion. While the same authors used montmorillonite as support, the present work employed H-ZSM-5, which exhibits high structural stability, together with a reductive treatment capable of inducing the formation of oxygen vacancies. In the study conducted by Rabie *et al.* (2017),[9] although Cu^0 favored CH_4 activation and alkaline cations assisted in the stabilization of CO_2 carbonates, the absence of an efficient redox pair, such as Ce^{3+}/Ce^{4+}, limited the CO_2 insertion capacity. In this case as well, the synthesis method differs from that adopted in the present work, since the authors carried out successive ion-exchange steps to introduce Cu and basic cations into zeolite, followed by reduction stages, resulting in Cu nanoparticles. In contrast, the methodology applied here ensured greater dispersion of active sites on the support surface. Moreover, Ding *et al.* (2007),[6] who studied Pd and Rh catalysts supported on SiO_2, relied on noble metals of high cost and limited availability. Such an approach, although efficient, is not competitive compared to the use of Zn, an abundant and low-cost element. The catalyst investigated in this work features oxygen vacancies in CeO_2, which are active for CO_2 adsorption, as well as active Zn species, effective in cleaving the C–H bond of CH_4, and the Brønsted acidity of H-ZSM-5 zeolite, which stabilizes acetate intermediates. Furthermore, the synthesis and reduction method differs from the conventional routes employed in MMT or ion-exchanged zeolites, ensuring higher metal dispersion and structural stability, even though the zeolite still retains a degree of ion exchange sufficient to generate the $Zn^{\delta+}$ species. These factors explain the productivity, which is up to four times higher compared with previously reported catalysts, while simultaneously eliminating the need for noble metals.

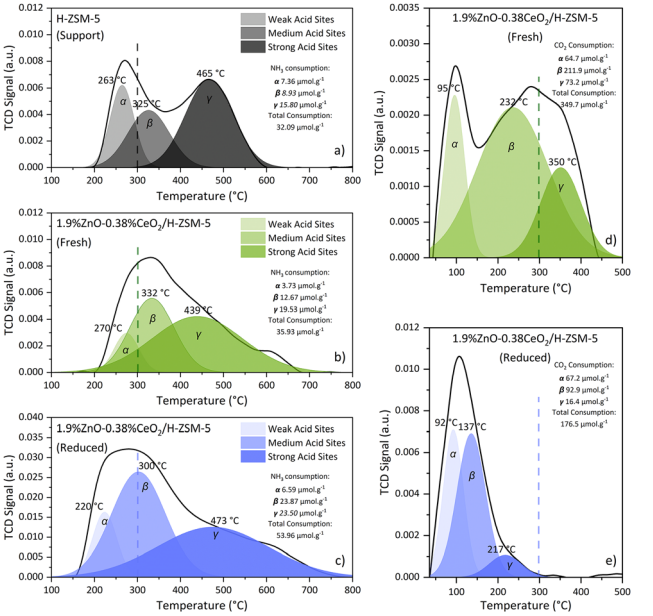

Fig. 7 Determination of weak, medium, and strong acid sites and ammonia consumption of the support (a), fresh catalyst (b), and reduced catalyst (c), and determination of basic sites and carbon dioxide consumption of the fresh (d) and reduced catalyst (e).

The acid sites present in the samples were evaluated through NH_3 temperature-programmed desorption (TPD-NH_3) profiles (Fig. 7).

The H-ZSM-5 support (Fig. 7a) exhibits desorption peaks at 263 °C, 326 °C, and 466 °C, corresponding to weak, medium, and strong acid sites, respectively,[28] with a total acidity of 32.09 μmolNH_3 g^{-1}. Upon modification with ZnO and CeO_2 (Fig. 7b), an increase in acidity is observed, with NH_3 consumption rising to 35.93 μmolNH_3 g^{-1} due to the introduction of new acid sites. In this context, ZnO acts as a Lewis acid, thereby altering the strength distribution of acid sites. The reductive treatment (Fig. 7c) causes the high-temperature desorption peak to shift to 473 °C, with increased intensity, and lower-temperature peaks at 220 °C and 300 °C become more prominent, indicating intensified acidity composed of medium and strong acid sites. The total ammonia uptake reached 53.96 μmolNH_3 g^{-1}.[29] The dashed line at 300 °C marks the reaction temperature, indicating the presence of weak, medium, and strong acid sites in both catalysts.

Changes in the basicity of the catalysts were evaluated through CO_2 temperature-programmed desorption (TPD-CO_2) analysis. The support exhibited no detectable basicity,[30] however, after ZnO and CeO_2 incorporation (Fig. 7d), the catalyst displayed desorption peaks at 96 °C, 231 °C, and 351 °C, with a total CO_2 uptake of 349.75 μmolCO_2 g^{-1}, attributed to the presence of CeO_2. After reduction (Fig. 7e), a decrease in basicity was observed, with a total CO_2 uptake of 176.49 μmolCO_2 g^{-1} and desorption peaks at lower temperatures (92 °C, 137 °C, and 217 °C).[31] The dashed line indicates that, in both the fresh and reduced catalysts, basic sites are present under the reaction conditions, although to a lesser extent in the reduced sample.

Thermogravimetric analysis (TGA) under an inert atmosphere (N_2) and Fourier Transform Infrared (FTIR) spectroscopy were employed to investigate the presence of acetic acid on the surface of the materials after the catalytic reaction. In Fig. 8a, referring to the reduced catalyst, the post-reaction sample exhibits a mass loss between 100 and 150 °C. This temperature range is typical for the decomposition of physically adsorbed or weakly bound acetic acid on the catalyst surface.[32] The difference compared to the support (Fig. 8c), which exhibits thermal stability in this region, reinforces the formation and retention of oxygenated compounds on the reduced catalyst. In Fig. 8b, corresponding to the fresh catalyst, the post-reaction sample shows a similar trend. However, the difference in the mass derivative intensity indicates a higher amount of adsorbed product on the reduced catalyst compared to the fresh one, due to the higher catalytic activity, as highlighted by the ^{1}H NMR and HPLC results. A joint analysis of the TPD-CO_2 and TGA profiles reveals that the reduced sample exhibits CO_2 desorption at low temperatures (Fig. 7e) and lower thermal stability of adsorbed carbonaceous species, consistent with the TGA results (Fig. 8a), showing more pronounced mass losses between 100 and 250 °C, a range associated with the decomposition of carboxylic species. These findings suggest that the surface of the reduced catalyst interacts weakly with acetic acid, facilitating its desorption. The FTIR spectrum (Fig. 8d) exhibits broad bands in the 2857–3010 cm^{-1} range, corresponding to O–H stretching,[33] which can be attributed to water or carboxylic acids. These bands are evident in the support, indicating the presence of water on the material surface as seen in Fig. 8c. For both the fresh and reduced catalysts, these bands are more intense, suggesting the formation of acetic acid, as also indicated by desorption at temperatures above 100 °C (Fig. 8b and a).

The X-ray photoelectron spectroscopy (XPS) analyses of fresh and reduced catalysts are shown in Fig. 9. Peaks related to Ce and Zn species are not visible in the survey spectra (Fig. 9a) due to low loadings, but high-resolution spectra of specific regions allow for analysis of these species. The spectra for the Si 2p (Fig. 9b) region show a peak centered at 103.3 eV, attributed to SiO_2 in the zeolite structure.[32]

Additionally, for the O 1s region (Fig. 9c), only one peak is observed, centered around 533.1 eV, attributed to oxygen in Si–O–Si or Si–O–Al sites of ZSM-5.[34] Since most oxygen on the surface comes from the zeolite structure, contributions from oxygen interacting with cerium and zinc cannot be clearly identified. From the Zn 2p spectra (Fig. 9d), two distinct surface species are observed in the fresh catalyst. The Zn species directly interact with the acid sites of the zeolite, forming $Zn(OH)^+$ sites, with a characteristic binding energy of 1023.2 eV.[35] The additional peak, located at 1022.3 eV, is likely due to small clusters of oxide within the zeolite's micropores, consistent with the binding energy of ZnO.[36] In the reduced sample, the peak at 1022.3 eV disappears, indicating that $Zn(OH)^+$ is the only Zn site present on the catalyst surface. The redispersion of ZnO clusters into Zn^{2+} species in $Zn(OH)^+$ sites is probably occurring through a reductive solid-state ion-exchange, as previously reported by In_2O_3/H-ZSM-5 material.[37] Since the initial metal impregnation in zeolite was not sufficient to completely exchange the Brønsted acid sites, ZnO is formed after calcination, as observed in the fresh catalyst. The reductive atmosphere promotes the migration of remaining ZnO clusters to neutralize Brønsted acid sites, resulting in the formation of additional Zn-exchanged sites. Under reaction conditions, $Zn(OH)^+$ species can be easily dehydrated and coupled with nearby Brønsted acid sites or terminal silanol groups to form mononuclear Zn^{2+} sites, which are

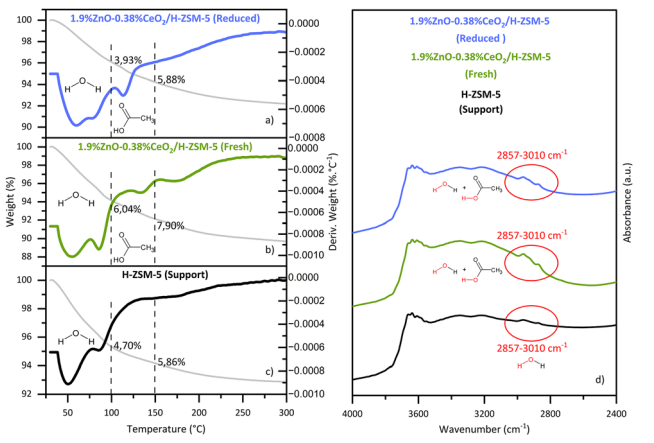

Fig. 8 TGA/DTG profiles under inert atmosphere (a–c) and FTIR spectra (d) of the post-reaction catalysts.

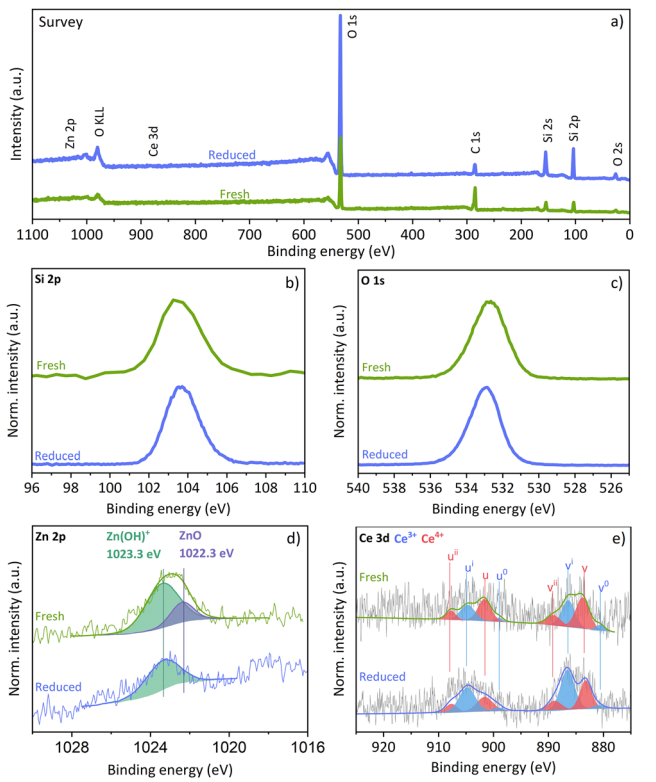

Fig. 9 X-ray photoelectron spectra of fresh and reduced 1.9%ZnO–0.38%CeO_2/H-ZSM-5 catalyst. (a) Survey scan, (b) Si 2p, (c) O 1s, (d) Zn 2p, and (e) Ce 3d levels.

reported to show better activity for CH_4 activation and stabilization of zinc methyl (Zn–CH_3) intermediate.[38] From the Ce 3d spectra (Fig. 9e), peaks v, u, v^{ii}, and u^{ii} are related to Ce(IV) $3d^94f^2$ O $2p^4$ and Ce(IV) $3d^94f^1$ O $2p^5$ final states, and peaks v^0, u^0, v^i, and u^i are related to Ce(III) $3d^94f^2$ O $2p^5$ and Ce(III) $3d^94f^1$ O $2p^5$ final states.[39,40] Comparing the surface composition of fresh and reduced catalysts (Table S1), it was clear that the contribution from Ce^{3+} species increased after catalyst reduction. The Ce^{3+}-enriched surface can potentially improve CO_2 adsorption, increase the density of adsorption sites, and stabilize adsorbed intermediates, such as carbonates.[41,42]

The estimation of the catalyst lifetime was evidenced by the decrease in acetic acid productivity over time (Fig. S7a), from 1273 μmol g^{-1} h^{-1} to 152 μmol g^{-1} h^{-1} within 20 hours. From the O_2 thermogravimetric analysis (Fig. S7b), it was confirmed that no mass losses consistent with the accumulation of carbonaceous matter occurred. In addition, the presence of adsorbed species in the material (carbonates, acetates, or oxygenated intermediates) cannot be ruled out, since they were not removed during the drying step after each reaction, despite having the potential to be eliminated during the reduction process or converted into other compounds under a reducing atmosphere. These species may occupy active sites or block micropores, which could be associated with the decrease in specific surface area revealed by N_2 physisorption (Fig. S7c), indicating physical changes in the support or at the catalytic interfaces that reduce the accessible area of active sites. Through HRTEM images of the post-reaction material (Fig. S8–S10), the deposition of carbon films or particles could be ruled out, corroborated by the O_2 thermogravimetric analysis previously shown. A significant decrease of Zn in the catalyst was also observed by EDS mapping, suggesting that Zn remained highly dispersed or partially exchanged in the zeolite; however, the active phase may have been leached during the multiple extraction processes[43,44] or may have sublimated[45] due to successive thermal treatments.

Finally, a mechanism for the formation of active sites in the reduced catalyst and to produce acetic acid is proposed in Fig. 10. As observed in XPS analysis, the presence of a reductive atmosphere led Brønsted acid sites (H^+) of ZSM-5 to be exchanged for Zn^{2+} ions in solid state, forming Lewis acid sites. This treatment resulted in the complete fragmentation of ZnO particles in the fresh catalyst. The CeO_2 deposited on the support is partially reduced from Ce^{4+} to Ce^{3+}, forming CeO_{2-x}, which is essential for CO_2 activation. Regarding the reaction mechanism, initially, CH_4 is adsorbed on the Lewis acid sites, where heterolytic cleavage of the C–H bond occurs, leading to the formation of zinc–methyl (Zn–CH_3) and zinc-hydroxyl (Zn–OH) species[4,8,46] while CO_2 is adsorbed and activated through interaction with oxygen vacancies in the lattice and Ce^{3+} centers, resulting in the formation of carbonate species (–COO^-), as evidenced by CO_2-DRIFTS (Fig. 2).[41,42] After activation, the methyl (CH_3–) and carbonate intermediates interact, promoting a C–C coupling that leads to the formation of an acetate-type intermediate (CH_3COO–).[47] Subsequent protonation of this intermediate, mediated by the proton released from the Zn–OH species formed in the initial step, along with electronic rearrangements, results in the formation of acetic acid (CH_3COOH).[5] Finally, the product desorbs from the catalytic surface, and the active sites of ZnO and CeO_2 are regenerated, thus completing the catalytic cycle. As demonstrated by the catalytic activity of the materials studied in this work, the Brønsted acidity (H^+) of the zeolite is of utmost importance for the kinetic mechanism of the reaction, as previously presented. To confirm this hypothesis, catalytic tests were carried out using the same proportions of ZnO and CeO_2 supported on a ZSM-5 zeolite in its sodium form. In this case, the acetic acid productivity was only 25.73 μmol g^{-1} h^{-1} for the fresh catalyst and 705.92 μmol g^{-1} h^{-1} for this catalyst in its reduced form, according to the ^1H NMR and HPLC analyses, confirming that the proton from the zeolite actively participates in the reaction and is essential for achieving higher yields.

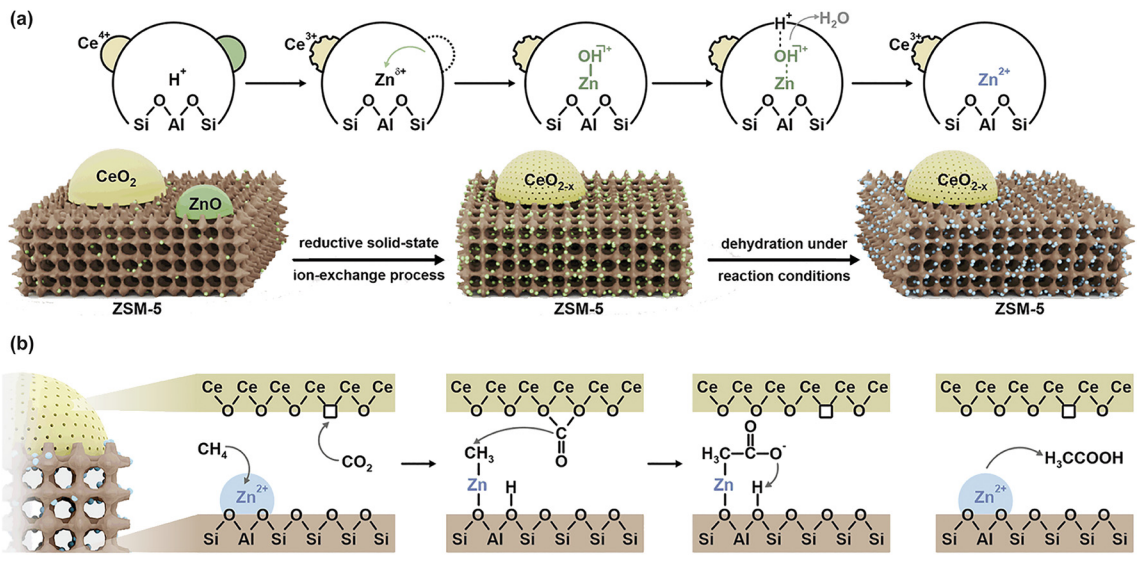

Fig. 10 (a) Proposed mechanisms for the formation of active sites in the reduced catalyst and (b) for the conversion of CH_4 and CO_2 into acetic acid.

Conclusions

Modifying zeolite with ZnO and CeO_2, especially in its reduced form, created a highly effective catalyst for acetic acid production. The reduction process with pure H_2 resulted in significant structural changes, such as the formation of oxygen vacancies that favor carbonate formation through CO_2 activation at Ce^{3+} sites and the formation of active Zn^{2+} species that assist in Zn–CH_3 formation during CH_4 adsorption. This is evidenced by an acetic acid productivity of 1473.4 μmol g^{-1} h^{-1}, confirmed by ^{1}H NMR, and a conversion rate of 35%. Although the conversion is relatively low, the yields surpassed those previously reported in the literature, even considering catalyst deactivation after multiple reduction and extraction cycles. Overall, these results highlight the potential of heterogeneous catalysis as a strategy for converting biogas into oxygenated compounds, combining catalytic efficiency with the reduction of greenhouse gas emissions.

Experimental

Catalyst preparation

The fresh catalyst was synthesized by the wet impregnation method. Five grams of commercial H^+-ZSM-5 were dispersed in 50 mL of deionized water and stirred for 6 hours at a rate of 600 rpm to ensure complete dispersion of the zeolite. After dispersion, nitrate solutions were added in sufficient amounts to achieve the desired oxide concentrations (0.38% CeO_2 (Aldrich - $Ce(NO_3)_3{\cdot}6H_2O$ 99%) and 1.90% ZnO (Synty - $Zn(NO_3)_2{\cdot}6H_2O$ PA) by mass) and the solution was stirred for an additional 6 hours. After the final dispersion, the solution was evaporated at 100 ± 5 °C to remove the excess aqueous solution and then dried in an oven at 95 ± 5 °C for 24 hours. The dried sample was ground and calcined in an oxidizing atmosphere with a heating rate of 2 °C min^{-1} up to 550 °C, maintaining the final temperature for 5 hours (Fig. S11).

For the reduced catalyst, in order to determine the optimal reduction temperature of the metal oxides impregnated on the support, a temperature-programmed reduction analysis (TPR-H_2) was conducted. Thus, the fresh catalyst was subjected to a reducing treatment with pure H_2. For this, 500 mg of catalyst were placed in a quartz tubular reactor. The system was initially purged with N_2 at 80 mL min^{-1} to remove air. Subsequently, reduction was carried out with a continuous flow of pure H_2 at 30 mL min^{-1}, under programmed heating at a rate of 10 °C min^{-1} up to 570 °C, and the final temperature was maintained for 1 hour to ensure complete reduction of the metal oxides. After the reducing treatment, the system was cooled to room temperature under N_2 flow and collected for reaction tests (Fig. S12).

Characterizations

The temperature-programmed reduction (H_2-TPR) was carried out using an automatic chemisorption analyzer (ChemiSorb 2750, Micromeritics) connected to a thermal conductivity detector (TCD), employing 300 mg of the previously calcined catalyst. The sample was purged with Ar at 25 mL min^{-1} for 30 minutes at 300 °C to remove adsorbed species. Then, the temperature was lowered to 25 ± 5 °C and the TPR test was started under a gas mixture of 10% H_2/Ar. The system was heated at a rate of 10 °C min^{-1} up to 800 °C.

X-ray Photoelectron Spectroscopy (XPS) was performed using a Scienta Omicron ESCA spectrometer equipped with a monochromatic Al Kα X-ray source (1486.6 eV) and a high-performance hemispherical analyzer (EAC-2000). Data processing was carried out using the Casa XPS software. The Shirley method was used to calculate the background in high-resolution spectra, and charging effects were corrected using the binding energy of adventitious carbon at 284.8 eV (Fig. S13). A Gaussian–Lorentzian function was employed for peak fitting.

In situ DRIFTS spectra of CO_2 adsorption on the catalyst surface were collected using a Shimadzu IRPrestige-21 FTIR spectrometer equipped with a Harrick cell. The experiment was conducted on the calcined and pre-reduced sample in a continuous flow system, as previously described. Prior to the measurements, the samples were pretreated by heating from room temperature to 300 °C (10 °C min^{-1}) under a N_2 flow of 20 mL min^{-1}, and the background spectrum was recorded. Subsequently, the N_2 flow was turned off, and the catalyst was exposed to a flow of 20 mL min^{-1} of pure CO_2 for 1 h, while spectra were collected during the adsorption of CO_2 on the surface of the materials.

X-ray diffraction (XRD) analysis was conducted using a Rigaku Ultima IV instrument at an acceleration voltage of 40 kV and an emission current of 20 mA, with Cu Kα radiation (λ = 1.5405 Å) and scanning in the 2θ range from 5° to 80° at 0.02° s^{-1}.

High-resolution transmission electron microscopy and elemental mapping by energy-dispersive X-ray spectroscopy were performed on a JEOL LaB6/JEM-2100 microscope at an operating voltage of 200 kV. A small amount of catalyst was dispersed in 1 mL of isopropanol using ultrasound for 15 minutes to ensure a homogeneous suspension. Then, a copper grid coated with a carbon film was gently dipped into the dispersed solution using anti-capillarity tweezers. The grid was left to dry at room temperature, allowing the solvent to evaporate completely before analysis.

Specific surface areas were determined by the BET method, using a Quantachrome NOVA 1000e instrument. 100 mg of catalyst was weighed into a previously weighed analysis cell and degassed under vacuum at 200 °C for 12 hours to remove adsorbed surface impurities such as water and gases. The sample was cooled to room temperature, and the cell weight was recorded after desorption. The analysis was performed at liquid nitrogen temperature (77 K). The volume of nitrogen adsorbed was measured as a function of relative pressure (P/P_0), ranging from vacuum to pressures close to nitrogen saturation. From the adsorption–desorption isotherm data, parameters such as specific surface area (using the BET method), pore volume, and pore size distribution (using methods such as BJH) were calculated.

NH_3 temperature-programmed desorption (TPD-NH_3), which evaluates acidic sites, was carried out using an automatic

chemisorption instrument (ChemiSorb 2750, Micromeritics) connected to a thermal conductivity detector (TCD). 100 mg of catalyst was pretreated in Ar at 300 °C for 30 minutes, then the temperature was lowered to 100 °C, followed by NH_3 chemisorption (1% NH_3/He) for 60 minutes, and subsequent He purging for 50 minutes. The TPD-NH_3 was performed in the temperature range of 100 ± 5 to 600 °C at a heating rate of 10 °C min^{-1} under He atmosphere.

CO_2 temperature-programmed desorption (TPD-CO_2) was performed on the same instrument. 100 mg of catalyst was pretreated in Ar at 300 °C for 30 minutes, then the temperature was lowered to 40 °C, followed by adsorption of pure CO_2 for 30 minutes and He purging for 50 minutes. The TPD-CO_2 was performed from 35 ± 5 to 600 °C at 10 °C min^{-1} under He atmosphere.

Thermogravimetric analysis (TGA) was carried out using a Mettler Toledo TGA/DSC instrument, with 10 mg of catalysts before and after reaction. Samples were placed in an alumina crucible and heated from 20 °C to 900 °C at a rate of 10 °C min^{-1} under a N_2 or synthetic air flow of 50 mL min^{-1}. This analysis was employed on samples after catalytic reaction to detect the presence of adsorbed acetic acid.

Infrared spectroscopy was conducted using a Shimadzu IRAffinity 1 FT-IR spectrometer. Ten milligrams of sample were placed in a diffuse reflectance accessory (praying Mantis-Harrick), and data were acquired at a resolution of 4 cm^{-1} over the spectral range of 400–4000 cm^{-1}.

Reaction tests

For catalytic conversion, a batch reactor (Parr 5500) was used. With 500 mg of catalyst, the reactor was heated to 300 °C under continuous N_2 flow and held at this temperature for 30 minutes to remove moisture from the catalyst surface. After this pretreatment step, the system was pressurized to 10 bar with an equimolar mixture of CH_4 and CO_2. The system was then sealed and stirred (600 rpm) for 5 hours. After the reaction, the system was cooled to 150 °C and then to room temperature using an ice bath to condense the reaction products. After cooling, the system was slowly degassed, and the catalyst was collected and transferred to a 50 mL Falcon tube. The reactor walls were washed with deionized water, and the reaction product was extracted with this solvent (Fig. S14). Following extraction, the sample was prepared for liquid-state proton nuclear magnetic resonance analysis (Bruker Avance III HD 600) and high-performance liquid chromatography (Shimadzu). These analyses allowed the calculation of the conversion (eqn (1)) based on the ratio between the amount of acetic acid produced and the CH_4 and CO_2 injected (eqn (1)) and the productivity (eqn (2)) based on the internal standard in the $_1$H NMR analysis and previous calibration in the HPLC.

$$\text{Conversion}\,(\%) = \left(\frac{C_{CH_3COOH}}{C_{CH_4/CO_2}}\right) \quad (1)$$

$$P\ (\mu\text{mol g}^{-1}\ \text{h}^{-1}) = \left(\frac{P_{\text{Analyte}} \cdot V_{\text{Extract}}}{V_{\text{NMR}} \cdot T_{\text{Reaction}} \cdot M_{\text{Cat}}}\right) \times 1000 \quad (2)$$

For the evaluation of the catalyst lifetime, batch reactions were carried out following the same procedure described previously. After each reaction, the catalyst was separated from the aqueous medium and dried in an oven at 100 ± 5 °C to remove the moisture adsorbed during the extraction process. The material was then subjected to reduction under a flow of pure H_2 to reactivate the catalytic sites. This reuse procedure was repeated three more times, totaling four consecutive reactions, covering a 20 hours cycle.

Author contributions

G. F. Lopes: Conceptualization, Methodology, Investigation, Formal analysis, Visualization, Writing – Original Draft. **A. F. Lucrédio**: Methodology, Validation, Investigation, Formal analysis, Writing – Review & Editing. **L. H. Vieira**: Conceptualization, Formal analysis, Writing – Review & Editing, Supervision, Project administration, Funding acquisition. **E. M. Assaf**: Conceptualization, Writing – Review & Editing, Supervision, Project administration, Funding acquisition.

Conflicts of interest

There are no conflicts to declare.

Data availability

All data supporting this article has been placed in the main text and SI. Additional description of experimental methods and supplemental data related to characterization (TEM, EDS, XPS, TGA, and N_2 physisorption) and catalytic activity (stability tests). See DOI: **https://doi.org/10.1039/d5nh00496a**.

Acknowledgements

The authors acknowledge the São Paulo Research Foundation (FAPESP) (Projects 2024/04540-4, 2022/06419-2, and 2022/10615-1) for financial support, the Nuclear Magnetic Resonance Laboratory at the Federal University of São Carlos (Prof. Dr. Tiago Venâncio) for assistance with the ^{1}H NMR analyses, and the Electrochemistry Group (Prof. Dra. Joelma Perez) at the Institute of Chemistry of São Carlos for support with the HPLC analyses.

Notes and references

1 A. Rafiee, K. R. Khalilpour, D. Milani and M. Panahi, *J. Environ. Chem. Eng.*, 2018, **6**, 5771–5794, DOI: **10.1016/j.jece.2018.08.065**.
2 J. Shan, M. Li, L. F. Allard, S. Lee and M. Flytzani-Stephanopoulos, *Nature*, 2017, **551**, 605–608, DOI: **10.1038/nature24640**.
3 T. Moteki, N. Tominaga and M. Ogura, *ChemCatChem*, 2020, **12**, 2957–2961, DOI: **10.1002/cctc.202000168**.
4 C. Tu, X. Nie and J. G. Chen, *ACS Catal.*, 2021, **11**, 3384–3401, DOI: **10.1021/acscatal.0c05492**.

5 Y. Li, K. Zheng, Y. Shen, M. Huang, B. Liu, Y. Xu and X. Liu, *J. Phys. Chem. C*, 2023, **12**, 5841–5854, DOI: **10.1021/acs.jpcc.3c01451**.
6 Y. Ding, W. Huang and Y. Wang, *Fuel Process. Technol.*, 2007, **88**, 319–324, DOI: **10.1016/j.fuproc.2004.09.003**.
7 N. Liu, N. Lu, K. Zhao, P. Liu, Z. Sun and J. Lu, *Chem. Eng. J.*, 2024, **487**, 150690, DOI: **10.1016/j.cej.2024.150690**.
8 R. Shavi, J. Ko, A. Cho, J. W. Han and J. G. Seo, *Appl. Catal., B*, 2018, **229**, 237–248, DOI: **10.1016/j.apcatb.2018.01.058**.
9 A. M. Rabie, M. A. Betiha and S.-E. Park, *Appl. Catal., B*, 2017, **215**, 50–59, DOI: **10.1016/j.apcatb.2017.05.053**.
10 Y. Wang, T. Du, Y. Song, S. Che, X. Fang and L. Zhou, *Solid State Sci.*, 2017, **73**, 27–35, DOI: **10.1016/j.solidstatesciences.2017.09.004**.
11 G. Zanelli, A. Lucredio, A. Sifuentes and E. Assaf, *Chem. Eng. Res. Des.*, 2023, **198**, 312–324, DOI: **10.1016/j.cherd.2023.09.005**.
12 B.-Z. Hsu, C.-L. Yu, S. Sakthinathan, T.-W. Chiu, B.-S. Yu, C.-C. Lin, L. Fan and Y.-H. Lee, *Catalysts*, 2023, **13**, 762, DOI: **10.3390/catal13040762**.
13 T. Kessaratikoon, S. Saengsaen, S. Del Gobbo, V. D'Elia and T. Sooknoi, *Catalysts*, 2022, **12**, 1533, DOI: **10.3390/catal12121533**.
14 G. Zhang, Y. Zhou, Y. Yang, T. Kong, Y. Song, S. Zhang and H. Zheng, *Molecules*, 2023, **28**, 3785, DOI: **10.3390/molecules28093785**.
15 B. Lu, F. Wu, X. Li, C. Luo and L. Zhang, *Carbon Capture Sci. Technol.*, 2024, **10**, 100173, DOI: **10.1016/j.ccst.2023.100173**.
16 O. D. A. S. Aldeen, M. Z. Mahmoud, H. S. Majdi, D. A. Mutlak, K. F. Uktamov and E. Kianfar, *Adv. Mater. Sci. Eng.*, 2022, 6165180, DOI: **10.1155/2022/6165180**.
17 L. Zhao, Y. Zhang, S. Bi and Q. Liu, *RSC Adv.*, 2019, **9**, 19236, DOI: **10.1039/C9RA03103K**.
18 S. Lu, Y. Ma and L. J. Zhao, *Mol. Liq.*, 2022, **364**, 119924, DOI: **10.1016/j.molliq.2022.119924**.
19 Y. Jia, J. Wang, K. Zhang, W. Feng, S. Liu, C. Ding and P. J. Liu, *Energy Chem.*, 2017, **26**, 540–548, DOI: **10.1016/j.jechem.2016.10.014**.
20 A. A. Ahmed and Z. H. Yamani, *Mater. Chem. Phys.*, 2021, **259**, 124181, DOI: **10.1016/j.matchemphys.2020.124181**.
21 S. Ravichandran, P. Thangaraj, P. Sengodan and J. Radhakrishnan, *Inorg. Chem. Commun.*, 2022, **146**, 110037, DOI: **10.1016/j.inoche.2022.110037**.
22 K. Punia, G. Lal, S. N. Dolia and S. Kumar, *Ceram. Int.*, 2020, **46**, 12296–12317, DOI: **10.1016/j.ceramint.2020.01.280**.
23 R. Manzorro, M. J. Montes-Monroy, D. Goma-Jiménez, J. J. Calvino, J. A. Pérez-Omil and S. J. Trasobares, *Mater. Chem. A*, 2022, **10**, 13074, DOI: **10.1039/d1ta08348a**.
24 L. L. Silva, B. R. Florindo, G. L. Catuzo, I. W. Zapelini, J. V. S. Cardoso, F. M. T. Luna, C. L. Cavalcante Jr. and L. Martins, *Mol. Catal.*, 2022, **529**, 112557, DOI: **10.1016/j.mcat.2022.112557**.
25 K. Nam, H. W. Ryu, M. Y. Gim and D. H. Kim, *Appl. Catal., B*, 2021, **296**, 120377, DOI: **10.1016/j.apcatb.2021.120377**.
26 S. M. Yusof, Z. B. Pang and L. P. Teh, *Mater. Today Proc.*, 2020, **31**, 155–160, DOI: **10.1016/j.matpr.2020.01.512**.
27 Z. Wang, Y. Li, Y. Wang, T. Li, J. Zheng, L. Huang, H. Zuo, D. Tian, H. Wang and K. Li, *Phys. Chem. Chem. Phys.*, 2025, **27**, 868, DOI: **10.1039/d4cp03370a**.
28 A. Parra-Marfil, R. Ocampo-Pérez, C. G. Aguilar-Madera, F. Carrasco-Marín, A. F. Pérez-Cadenas, A. Bueno-López and E. Bailón-García, *Environ. Sci. Pollut. Res.*, 2024, **31**, 32766–32783, DOI: **10.1007/s11356-024-33327-5**.
29 C. Auepattana-aumrung, S. Wannapaiboon, S. Wannakao, S. Praserthdam, B. Jongsomjit, J. Panpranot and P. Praserthdam, *Mol. Catal.*, 2022, **529**, 112533, DOI: **10.1016/j.mcat.2022.112533**.
30 R. Liu, Z. Ma, J. D. Sears, M. Juneau, M. M. Neidig and M. D. J. Porosoff, *J. CO_2* Util., 2020, **41**, 101290, DOI: **10.1016/j.jcou.2020.101290**.
31 L. Szkudlarek, K. Chałupka, W. Maniukiewicz, J. Albinska, M. I. Szynkowska-Józwik and P. Mierczynski, *Catalysts*, 2021, **11**, 1260, DOI: **10.3390/catal11111260**.
32 M. S. Hofman, E. V. Scoullos, J. P. Robbins, L. Ezeonu, D. V. Potapenko, X. F. Yang, S. G. Podkolzin and B. E. Koel, *Langmuir*, 2020, **36**, 8705–8715, DOI: **10.1021/acs.langmuir.0c00713**.
33 R. C. Ong and T.-S. J. Chung, *Membr. Sci.*, 2012, **394–395**, 230–240, DOI: **10.1016/j.memsci.2011.12.046**.
34 L. H. Vieira, K. T. G. Carvalho, E. A. Urquieta-González, S. H. Pulcinelli, C. V. Santilli and L. Martins, *J. Mol. Catal. A: Chem.*, 2016, **422**, 148–157, DOI: **10.1016/j.molcata.2015.12.019**.
35 M. J. Valero-Romero, S. Sartipi, X. Sun, J. Rodríguez-Mirasol, T. Cordero, F. Kapteijn and J. Gascon, *Catal. Sci. Technol.*, 2016, **6**, 2633–2646, DOI: **10.1039/C5CY01942G**.
36 K. Wang, M. Dong, X. Niu, J. Li, Z. Qin, W. Fan and J. Wang, *Catal. Sci. Technol.*, 2018, **8**, 5646–5656, DOI: **10.1039/C8CY01734D**.
37 Y. Yuan, E. Huang, S. Hwang, P. Liu and J. G. Chen, *Nat. Commun.*, 2024, **15**, 6529, DOI: **10.1038/s41467-024-50709-y**.
38 J. Xu, A. Zheng, X. Wang, G. Qi, J. Su, J. Du, Z. Gan, J. Wu, W. Wang and F. Deng, *Chem. Sci.*, 2012, **3**, 2932–2940, DOI: **10.1039/C2SC20434G**.
39 M. A. Rossi, L. H. Vieira, L. F. Rasteiro, M. A. Fraga, J. M. Assaf and E. M. Assaf, *React. Chem. Eng.*, 2022, **7**, 1589–1602, DOI: **10.1039/D2RE00033D**.
40 L. H. Vieira, J. M. Assaf and E. M. Assaf, *Mater. Lett.*, 2020, **277**, 128354, DOI: **10.1016/j.matlet.2020.128354**.
41 L. F. Rasteiro, R. A. De Sousa, L. H. Vieira, V. K. Ocampo-Restrepo, L. G. Verga, J. M. Assaf, J. L. F. Da Silva and E. M. Assaf, *Appl. Catal., B*, 2022, **302**, 120842, DOI: **10.1016/j.apcatb.2021.120842**.
42 S. Zhang, Z. Tian, Y. Ma and Y. Qu, *ACS Catal.*, 2023, **13**, 4629–4645, DOI: **10.1021/acscatal.2c06351**.
43 S. Sharma, G. K. Agarwal and N. N. Dutta, *J. Mater. Cycles Waste Manage.*, 2020, **22**, 1509–1520, DOI: **10.1007/s10163-020-01038-x**.
44 H. A. Aziz, R. Yusoff, N. G. Cheng, Z. Idris and N. A. S. Ramli, *J. Surfact Deterg.*, 2023, **26**, 477–490, DOI: **10.1002/jsde.12648**.
45 A. Bonnin, Y. Pouilloux, V. Coupard, D. Uzio and L. Pinard, *Appl. Catal., A*, 2021, **611**, 117976, DOI: **10.1016/j.apcata.2020.117976**.
46 V. B. Kazansky, A. I. Serykh and E. A. Pidko, *J. Catal.*, 2004, **225**, 369–373, DOI: **10.1016/j.jcat.2004.04.029**.
47 Y. Zhao, H. Wang, J. Y. Han, X. Zhu, D. Mei and Q. Ge, *ACS Catal.*, 2019, **9**, 3187–3197, DOI: **10.1021/acscatal.9b00291**.

